

Features of Synthesis of $Y_2Ti_2O_7$ Ceramics for the Purpose of Obtaining Dispersion-Strengthened Steels

E.S. GEVORKYAN^a, V.P. NERUBATSKYI^a, R.V. VOVK^b,
V.O. CHYSHKALA^b, S.V. LYTOVCHENKO^b,
O.M. MOROZOVA^a AND J.N. LATOSIŃSKA^{c,*}

^aUkrainian State University of Railway Transport, Feierbakh sq. 7, Kharkiv, 61050, Ukraine

^bV.N. Karazin Kharkiv National University, Svobody sq. 4, Kharkiv, 61022, Ukraine

^cAdam Mickiewicz University, Faculty of Physics, Uniwersytetu Poznańskiego 2, 61-614 Poznań,

Received: 27.06.2022 & Accepted: 17.10.2022

Doi: [10.12693/APhysPolA.142.529](https://doi.org/10.12693/APhysPolA.142.529)

*e-mail: jolanta.latosinska@amu.edu.pl

The method of electron beam heating of a mixture of yttrium and zirconium oxides for the synthesis of complex oxides has been implemented. It is established that the applied technology of melting the mixture of oxides leads to the formation of fluorite phases. It is determined that homogenization of the initial mixture of oxides should be carried out in a high-energy mill, which will reduce the temperature and duration of the synthesis of complex oxide compounds, including the desired structure of pyrochlorine. It is proposed to improve the technique of intensive thermal influence on the process of pyrochlorine synthesis by using an equiatomic alloy Y–Ti (65 wt.% Y–35 wt% Ti), which has been smelted using the arc melting method in an argon atmosphere. It was found that hydrogen saturation reduces the efficiency of pyrochlorine synthesis and increases the grain size, which may be associated with grain growth at the stage of hydrogen saturation.

topics: DSO-steel, oxide, pyrochlorine, melting

1. Introduction

For the stable and sustainable development of human civilization, the issues of energy resources, energy production and energy are crucial. Given the potential limitations of minerals, the constant increase in energy consumption and the desire not to worsen the environmental situation poses new challenges for the energy industry. The development of environmentally friendly technologies contribute to the formation of sustainable production [1].

The prospects for civilian nuclear energy are still unclear, but it is safe to say that nuclear reactors are guaranteed to be built and used as long as ships and submarines, equipped with nuclear power plants and nuclear weapons, remain relevant. This means that the development of new reactor technologies is still relevant and necessary. The modern nuclear industry faces many challenges, for example, development of new reactor systems or technological implementation of those already developed, conservation of decommissioned nuclear facilities, disposal of radioactive waste, etc.

Further economically justified, socially attractive and technologically safe use of nuclear technologies and the operation of modern complex technical

facilities, which undoubtedly include nuclear power devices, and the further development of nuclear, and in the future thermonuclear energy, are impossible without modernization of the known and the creation of new fuel and construction materials for the nuclear reactors core. One possible way to improve or create new nuclear materials is through the use of nanotechnology.

In addition to the creation of structural materials with high radiation resistance for thermal reactors, there is another important area among the prospects for nuclear energy development, namely the transition to the use of fast neutron reactors, for efficient and long-term reliable operation, which must increase fuel burnout. Such reactors also require materials that will have better quality properties compared to already implemented materials in terms of radiation swelling, radiation creep, high- and low-temperature radiation embrittlement, as well as the radiation stability of the structure under neutron irradiation.

A promising direction in the development of materials for the nuclear industry is the creation of composite materials based on ferritic-martensitic radiation-resistant steels. Such materials are DSO-steels alloys, the steel matrix of which is

strengthened by nanosized particles of oxides (simple or complex) [2]. DSO-steels show excellent radiation resistance compared to other traditional heat-resistant steels and austenitic steels, making them promising materials for in-vessel elements of thermal reactors, fast neutron reactor shells, supercritical reactors with pressurized water reactors and the first wall. The oxide nanoparticles, which are dispersed in the volume of DSO-steels, perform a number of important functions. Firstly, these particles act as the barrier to the free movement of dislocations and migration of the grain boundaries, which increases tensile strength and improves creep resistance. Secondly, the oxide particles provide efficient absorption of radiation-induced defects (vacancies and interstitial atoms). Thirdly, these particles implement a simplified process of formation of helium bubble embryos, which suppresses the process of bubble formation and thus provides increased resistance to radiation. All this increases the stability of the structural elements of the material under irradiation, and consequently improves the material radiation resistance.

The materials with the pyrochlorine structure are multifunctional and can be used to solve many of the above-mentioned problems. Pyrochlorines are refractory materials with important properties including ionic conductivity [3, 4], optical nonlinearity [5], high radiation resistance [6] etc. Potential applications of pyrochlorine include thermal barrier coatings [7], dielectrics with high dielectric constant [8], solid electrolytes, anodes and cathodes in solid oxide fuel cells [9], materials for the safe disposal of some nuclear waste [10]. In addition, pyrochlorines have potential as ceramic pigments taking into account their high melting point, high refractive index and ability to accept impurities of transition metals [11].

From the large family of pyrochlorines, special attention is paid to obtaining and studying the possibility of using titanate and zirconate pyrochlorines.

Thus, the study [12] showed that in $Y_2Zr_2O_7$ at relatively low Mn-doping (from 2.5 to 10%), bulk conductivity increased at low temperatures (due to the introduction of electronic charge carriers in the lattice), and, in turn, at high temperatures — ionic conductance. The conductivity values measured for these $Y_2Zr_2O_7$ formulations in this study ($8.3 \times 10^{-3} \text{ S cm}^{-1}$) are much lower than those of traditional electrolytes. However, in the form of thin, dense and compact layers with a thickness of 20–50 μm , in the case of traditional electrolytes, it is possible to realize higher conductivity, which will allow the use of pyrochlorine as an alternative electrolyte material with Ni–YZ metal-ceramic anode in solid oxide fuel cells of transitional temperatures.

The study [13] showed that $Gd_2Zr_2O_7$ (GZO) coating showed excellent thermal conductivity in relation to 7YSZ (7 wt% yttrium stabilized zirconia), but the rate of erosion has increased by an order

of magnitude. For design and service life reasons, this may preclude the use of GZO coatings in certain areas. In addition, layered coatings with rare earth doped (Yb and Gd) yttria stabilized zirconia (*t'* Low-*k*) and GZO were studied. Despite the fact that the degree of erosion has been halved, the use of such coatings has been questioned due to diffusion processes. The mechanical characteristics of the surface (hardness, microhardness) are a qualitative criterion for the wear resistance of coatings during abrasive wear, including the case of simultaneous thermal exposure [14].

The study [15] showed that a computational thermodynamic modeling approach was used to predict the phase stability of the pyrochlorine phase in the ZrO_2 – Gd_2O_3 – La_2O_3 system for high-temperature thermobarrier coatings in gas turbine engines.

The study [16] showed that the synthesis of the $Y_2Zr_2O_7$ pyrochlorine substrate was carried out by coprecipitation ($Y_2Zr_2O_7$ –CP), burning of glycine nitrates ($Y_2Zr_2O_7$ –GNC) and hydrothermal ($Y_2Zr_2O_7$ –HT) methods. Pyrochlorine was used as a matrix for Ni (10 at.% nickel is at the Y position in pyrochlorine). This system was used as a catalyst for the steam reforming of methane to produce hydrogen.

The fundamental thermal properties of pyrochlorines are also noteworthy. The studies include molecular-dynamic modeling of thermal conductivity [17], theoretical studies of the structure and thermal conductivity of $La_2Zr_2O_7$ [18] and experimental determinations of the enthalpies of titanate pyrochlorine formation [19].

Yttrium dithitanate, $Y_2Ti_2O_7$, is a particularly important member of the pyrochlorine family. The fact that $Y_2Ti_2O_7$ is diamagnetic makes it one of the most acceptable pyrochlorines for detailed study. This pyrochlorine is also considered as a buffer layer on superconducting substrates [20].

The study [21] showed a comprehensive analysis and investigation of the mechanical properties and characteristics of $Y_2Ti_2O_7$ pyrochlorine compared to the properties of the original oxides of TiO_2 and Y_2O_3 . The $Y_2Ti_2O_7$ ceramics with fine ($0.9 \pm 0.3 \mu\text{m}$) and equiaxed grains were made according to the methods of solid-phase reaction and hot pressing. The low strength of $Y_2Ti_2O_7$ ceramics is due to its high natural fragility [22].

The study [23] showed that glass-ceramic (pyrochlorine $Y_2Ti_2O_7$) was fabricated by calcining a mixture of glass precursor powder and (YTi)-composite that was produced by a soft chemistry route. The phase pure pyrochlorine was crystallized *in-situ* in the amorphous glass matrix at 1200°C with dwelling time over 1 h. Minor impurities were only observed at a higher ceramic content by this new method, which was superior to the mixed-oxide route. It can be concluded that the processing conditions of this method were very flexible for the production of $Y_2Ti_2O_7$ pyrochlorine GCs as potential waste forms for actinides. Together with other

advantages (e.g., no need for an organic solvent in chemical synthesis or the milling of reactant powders), this route may provide an alternative mean to fabricate glass-crystal ceramics without requiring the formation of fully crystallized ceramics and finely ground parent glass before mixing and is very robust and attractive for scaleup production.

The study [24] showed that the $Y_2Ti_2O_7$ transparent ceramic was fabricated by reactive sintering using spark plasma sintering at 1673 K for 2.7 ks. The sintered body exhibited a cubic pyrochlore structure and a uniform microstructure with an average grain size of 2.9 μm . The transmittance reached 73% at a wavelength of 2000 nm after annealing at 1023 K for 21.6 ks.

The study [25] showed that the single crystals of $Y_2Ti_2O_7$ were grown using OFZ technique having four mirrors (FZ-T-4000-H-HR-I-VPO-PC) under a continuous flow of air at the flow rate of 0.25 l/min. Prior to growth, polycrystalline $Y_2Ti_2O_7$ powders were synthesized by solid state reactions using high pure chemicals Y_2O_3 (99.995%) and TiO_2 (99.95%). High optical transparency with 3.44 eV optical band gap ensures crystal quality as well. For the first time, the hardness, elastic and bulk modulus of $Y_2Ti_2O_7$ single crystals are measured using nanoindentation, and the values are found to be higher as compared to available literature reports.

Along with the general studies on this pyrochlorine, studies of phase stability [26], thermal properties [27], modeling to predict structural, electrical and plastic properties [28] and others have been carried out.

Very important, although specific, is the use of pyrochlorines in the creation of high-strength and radiation-resistant steels of the so-called DSO class (dispersion strengthened by oxides). Standard technology of manufacturing such steels consists in mechanical alloying of steel powder with nano-dispersed yttrium oxide in the amount of 0.3–0.5% by volume. As a result of intensive mechanical grinding, the nano-dispersed yttrium powder dissolves in the steel matrix. In the process of further mechanical and thermal processing of workpieces made of such mechanically doped powder (for example, hot isostatic pressing), emissions in the nanoscale appear in $Y_2Ti_2O_7$ (titanium is present in the source steel in solid solution). Due to the high selection density, the small size of allocations, and the specific structure of the boundaries of the matrix-selection, said allocations serve both as effective drains of radiation defects and effective stoppers for mobile dislocations. As a result, steel is formed which has high values of strength and radiation resistance [29, 30]. In some cases, mechanical doping with yttrium oxide is replaced by doping with $Y_2Ti_2O_7$ pyrochlorine nanoparticles, which leads to a more uniform distribution of nanoparticles in the steel and improved mechanical properties.

In the study [31], $Y_2Ti_2O_7$ nanoparticles with a size of 72 ± 15 nm were obtained by annealing Y–Ti hydrides at 900°C for 1 h, and then added as an input powder to obtain DSO-steels containing aluminum. $Y_2Ti_2O_7$ particles did not decompose but transformed into amorphous clusters during mechanical doping. In comparison with relatively large (5–100 nm) particles of Y–Al–O oxides in DSO-steels containing aluminum obtained using mechanical doping of Y_2O_3 nanopowders, doping with $Y_2Ti_2O_7$ nanopowders leads to a much smaller average size of oxide emissions in steel (7.4 ± 3.7 nm) and their high (emissions) density, which is $(7.3 \pm 0.6) \times 10^{22} \text{ m}^{-3}$. In addition, the $Y_2Ti_2O_7$ nanoparticles had a semi-coherent interface with the ferrite matrix. Tensile strength and uniform elongation of DSO-steels with the addition of 0.2 wt% and 0.6 wt% $Y_2Ti_2O_7$ were better than with the addition of 0.35 wt% Y_2O_3 .

The study [32] concerned the microstructure of steel 08X18H10T, which was strengthened by nanoparticles of 80% Y_2O_3 –20% ZrO_2 . After cold compaction, spinning and subsequent annealing at 1000°C, a uniform distribution of nanoparticles with a characteristic size of about 10 nm and a bulk density of $7 \times 10^{21} \text{ m}^{-3}$ in the matrix phase was observed. It was shown that the precipitates preferably have a crystal lattice $Y_2(Ti_{1-x}Zr_x)_2O_7$ (pyrochlorine).

The study [33] concerned the features of austenitic DSO-steel 08Cr18Ni10Ti after mechanical doping with Y_2O_3 – ZrO_2 nanooxides. There was a tendency to reduce the size of crystallites and increase the level of microdeformation with increasing the yttrium content in the input oxide nanopowders. The highest density of precipitates, smaller average size and higher homogeneity of its size distribution were found in the sample doped with 80 mol% Y_2O_3 –20 mol% ZrO_2 nanooxides. The strength characteristics of DSO-steel after doping with nanooxides of 80 mol% Y_2O_3 –20 mol% ZrO_2 are much higher than that of base steel. A particularly significant increase is observed at high temperatures (700°C), where the yield strength of DSO-steel is 2.3 times higher than in the original steel 08Cr18Ni10Ti. At the same time, plasticity decreases slightly, but remains at a sufficient level for technological and operational purposes.

In the study [34], the swelling of DSO-steel X18H10T (0.5 wt% of oxides nanopowders with the composition of 80 mol% Y_2O_3 and 20 mol% ZrO_2) after irradiation with Cr^{3+} ions with 1.8 MeV at temperatures of 500–650°C to doses of 50–100 dpa. It was found that the swelling of DSO-steel in the studied temperature range does not exceed 5%, which is lower than that of ordinary steel (over 8%). The curve of swelling at irradiation up to 50 dpa has no extremes in all temperature range of irradiation.

Thus, the problem of creating DSO-steels with improved properties is part of the overall problem of creating heterogeneous solids with the given

properties, provided by the implementation of the required structural and phase state of both components and the whole object. Taking this into account, all stages of the formation of such materials were investigated, from the initial formation of dispersed components to the implementation of the desired structural and phase state of the whole composite [35–38]. This is facilitated by the accumulated experience in the synthesis of oxide compounds in the form of ultrafine and nanodisperse powders, the study of structural–phase transformations in them during compaction and consolidation [39–42].

2. Experimental

In the first stage of sample preparation, the initial industrial powders ZrO_2 and Y_2O_3 were taken in a ratio of 1:1 (atomic %) and mixed up in a mixer for 2–8 h. After homogenization of the mixture, it was compacted into tablets on a mechanical press in a steel mold in air at an excess pressure of 1.2 GPa, after which the tablets were subjected to heat treatment (initial consolidation by sintering) to ensure some mechanical strength and prevent breakage during further processing. The temperature and duration of sintering were experimentally chosen to be the lowest to prevent phase transformations in the compacts. The samples were then placed in a tantalum basket container and fixed in a vacuum device for further exposure to high temperature. Estimates performed taking into account the actual geometry of the device showed that for the synthesis of high-temperature compounds at temperatures up to 3000° with a container surface area of $3\text{--}5\text{ cm}^2$ and the reflection efficiency of infrared mirrors at 40% (return of energy), the discharge current must exceed 2 A at 150 V and more. The operating pressure at the inlet of the working gas to the chamber should be maintained at 1.2×10^{-3} Torr, and at the inlet to the thermocathode region — 3.5×10^{-4} Torr. The magnetic field strength in the maximum in both cases of gas supply should be 450 E. The distance from the container to the outlet of plasma source should not exceed 20 cm, which corresponds to a maximum magnetic field strength of 450 E.

The next step was to heat the thermocathode, which was realized by flowing a direct current through it due to the release of Joule heat. The cathode heating process took into account the change in the electrical resistance of the cathode with the increase of its temperature and the corresponding change in the amount of heat released, as well as the gradual increase in energy consumption for radiation and emission from the cathode. Since the emission current of the thermocathode is determined by its temperature (i.e., the corresponding current through the cathode), in order to prevent the cathode tungsten wire from burning, the electrical parameters of the discharge also gradually

increased, starting from a starting discharge voltage of 100 V. The current through the cathode was gradually increased. Subsequently, the cathode incandescent current was slowly increased until the required discharge current was reached at the level of 0.5–1 A. The incandescent current was 35–37 A. Continuing to increase the cathode incandescent current, the discharge current was adjusted to 2 A and the discharge voltage was kept at 200 V. After the stable mode of the plasma jet was achieved, power was supplied to the container. In the process of sample heating, the voltage on the container was 1 kV and the current reached 100 mA. After reaching the temperature at which intense release of steam and gases began, an area of ionic plasma was formed above the container, the glow of which could be observed and monitored visually. The glow had a blue color due to the corresponding ionic and elemental composition of the gas-plasma medium. The duration of high-temperature exposure in the experiments was 5 min.

After that, the discharge voltage was switched off on the crucible, the incandescent current was gradually reduced until it was completely switched off, the magnetic field was switched off and the working gas flow was blocked. The system was kept at residual pressure for five minutes to cool the sample, after which air was pumped into the pump-sealed chamber and the sample was removed.

The structural-phase state of the samples was examined on an electron microscope JEOL JSM-7001F SEM to obtain images of microstructure and cartography, as well as on X-ray diffractometers DRON-2.0 and DRON-4-07.

3. Result and discussion

The image of the microstructure obtained as a result of the structural-phase state of the samples is shown in Fig. 1.

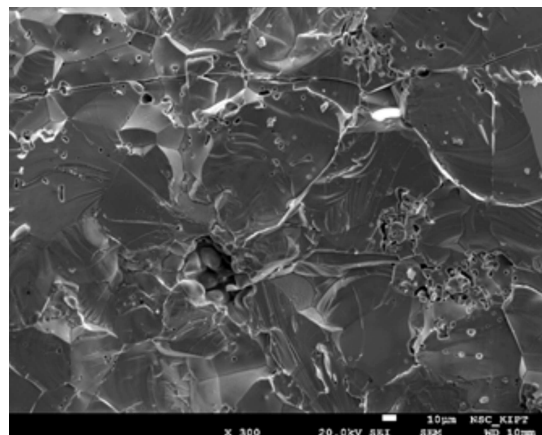


Fig. 1. Microstructure of the fracture site of the sample after melting, which analyzed the elemental composition.

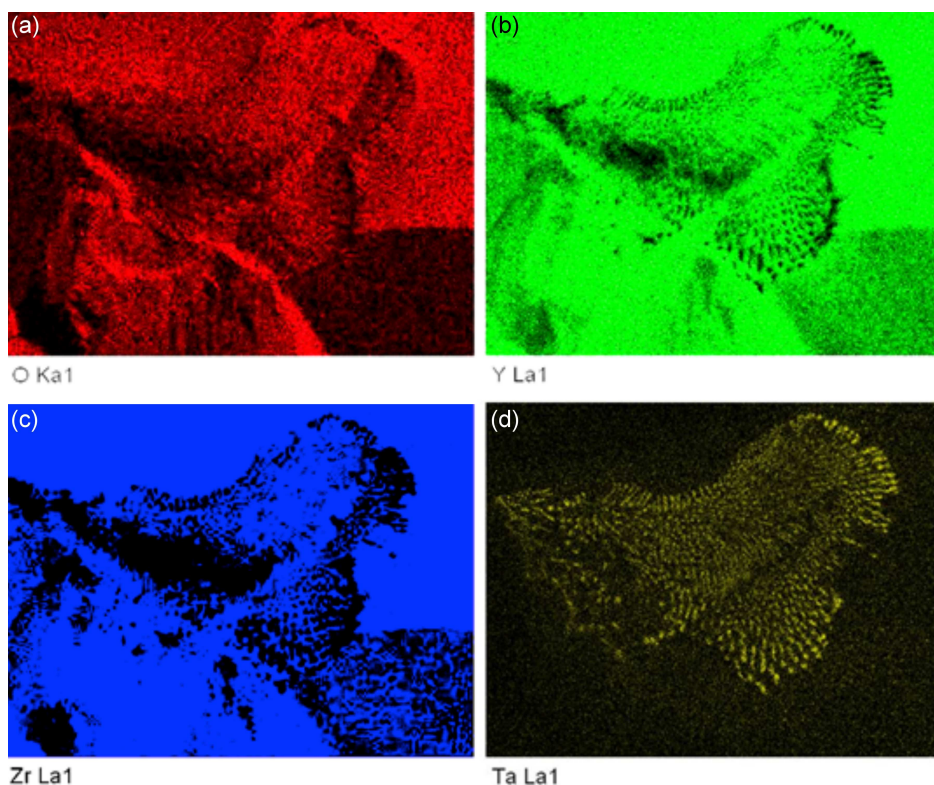


Fig. 2. Distribution of elements on the fracture surface of the sample after melting: (a) oxygen, (b) yttrium, (c) zirconium, (d) tantalum.

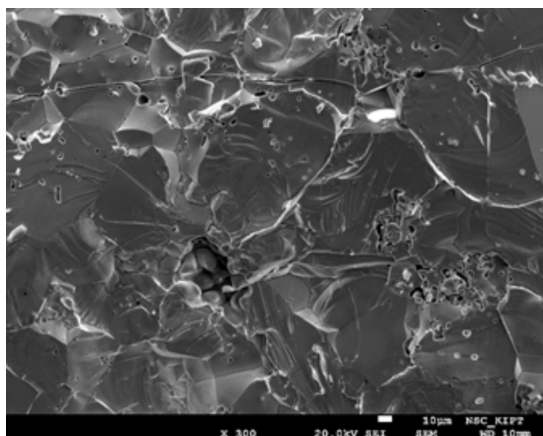


Fig. 3. Melted sample fracture microstructure.

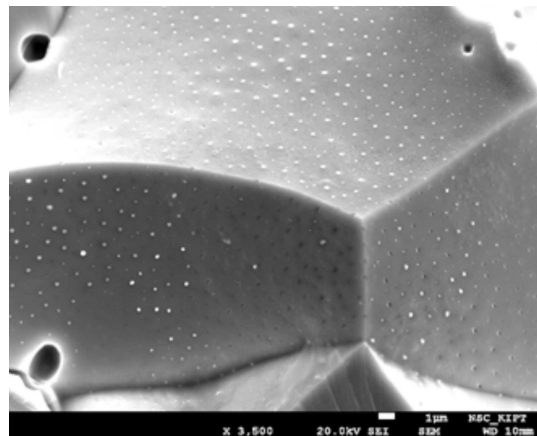


Fig. 4. Fracture surface of the sample with Ta_2O_5 emissions.

The distribution of elements on the fracture surface of the sample after melting is shown in Fig. 2. To simplify the analysis, the obtained images are presented in one scale. The obtained data show that the initial powders of zirconium and yttrium oxides are well mixed. The zones of presence of these elements practically coincide (Fig. 2a–c). Only tantalum oxide is released at the fracture (Fig. 2d).

The structure of the obtained alloy is represented mainly by large grains of $100\ \mu\text{m}$, which are characteristic of the melted ceramics (Fig. 3), although part of the volume consists of smaller grains.

At high magnifications, the release of tantalum oxide is noticeable, which during the crystallization of the melt does not dissolve in the mixture of oxides, and in some areas is released in the form of regularly distributed fibers (Fig. 4).

The qualitative phase analysis was performed according to the file of the international database ICDDPDF-2. The quantitative phase analysis of the samples and the determination of the phase lattice parameters was performed by the Rietveld method.

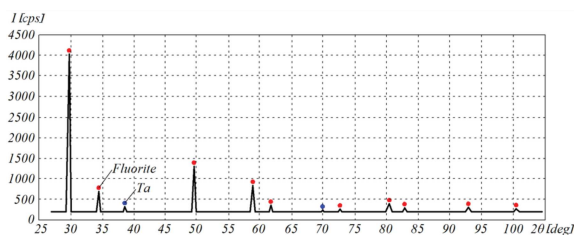


Fig. 5. Molten sample diffraction pattern.

TABLE I

Distribution of elements on the melted sample fracture surface.

| Element | Mass % | Atomic % |
|---------|--------|----------|
| O | 26.85 | 67.95 |
| Y | 38.36 | 17.47 |
| Zr | 30.85 | 13.69 |
| Ta | 3.95 | 0.88 |

The diffraction pattern of the sample (Fig. 5) revealed lines of two phases — fluorite ($(Y, Zr)O_x$ and tantalum oxide (substrate). The parameter of the fluorite lattice is $a = 5.206 \text{ \AA}$.

According to the elemental analysis (Table I), the ratio of the oxides Y and Zr in the alloy approximately corresponds to the initial mixture (within the device inaccuracy).

Additional annealing at 1200°C for 7 h did not lead to the formation of pyrochlorine phase in heat. Only two phases of fluorite with lattice parameters 5.2 and 5.217 \AA and the tantalum oxide phase were recorded (Table II, Fig. 6).

The analysis of the obtained data shows that the applied technology of melting the mixture of oxides leads to the formation of fluorite phases. The phase with pyrochlorine structure, the formation of which is more attractive due to better structural compatibility with Fe, is not fixed in the final material even after additional heat treatment. The reasons for this may be better thermodynamic characteristics and stability of the fluorite phases formed from the mixture of the tested composition, compared with similar indicators of pyrochlorine phases, the synthesis of which is potentially possible.

Thus, for the synthesis of the pyrochlorine phase, a number of conditions must be met, in particular:

1. based on the analysis of phase diagrams, it is necessary to clearly determine the interval of compositions in which the existence of the pyrochlorine phase is possible and, in accordance with these data, prepare mixtures of oxides;
2. homogenization of the oxides initial mixture should be carried out in a high-energy mill, which will reduce the temperature and duration of the synthesis of complex oxide compounds, including the desired structure of pyrochlorine;

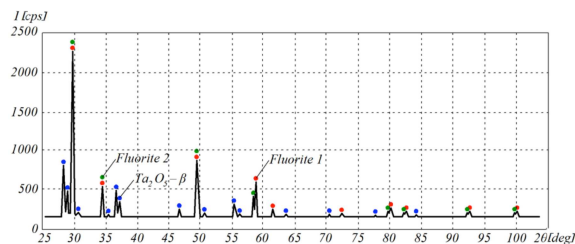


Fig. 6. Diffractogram of the melted sample after additional annealing.

TABLE II

Phase composition of the melted sample fracture surface after additional annealing.

| Phase | Content [wt%] | Lattice parameters [\AA] |
|-------------------------------|---------------|---|
| Fluorite 1 | 48.6 | 5.2 |
| Fluorite 2 | 30 | 5.217 |
| $\beta\text{-Ta}_2\text{O}_5$ | 21.4 | $a = 43.966$; $b = 3.889$; $c = 6.189$ |

3. the technology of high-energy thermal impact on the initial powder mixture needs to be improved to significantly improve the temperature control of the process;
4. it is necessary to provide a controlled change in the composition of the sample due to evaporation of elements in the technology of high-energy thermal influence, without which it is impossible to correctly determine the initial composition of mixtures.

The fulfillment of the first condition is complicated by the implementation of highly nonequilibrium conditions in the experiment, which usually lead to a very significant distortion of traditional equilibrium state diagrams.

The second condition is related to the further improvement of the technique of intensive thermal influence on the synthesis of pyrochlorine and can be realized by using the equiatomic alloy Y–Ti (65 wt% Y–35 wt% Ti), which it was smelted by arc melting in argon. Metallographic studies showed the complete absence of mixing and crystallization of titanium with spherical droplets with yttrium, as shown in Fig. 7.

Part of the obtained ingot was used to obtain fast-hardened strips by spinning, which realizes the nanostructured state of the alloy. The tapes have high fragility. Some of the tapes were saturated with hydrogen at $450\text{--}500^\circ\text{C}$. Conditions for processing the samples are given in Table III.

Figure 8 shows the thermogravimetric curves of samples no. 1 and no. 7.

The onset temperature of the reaction in the fast-hardened strips, saturated with and without hydrogen, is approximately the same and equals $450 \pm 20^\circ\text{C}$. However, intensive oxidation of

TABLE III

Conditions for processing the samples.

| Sample no. | Description of the sample | Research |
|------------|---|----------|
| 1 | Tapes after fast hardening (second-hand) | TGA, XRD |
| 2 | w/h + annealing 900°C for 3 h | XRD |
| 3 | w/h + annealing 950°C for 3 h | XRD |
| 4 | w/h + annealing 1000°C for 3 h | XRD |
| 5 | w/h + annealing 1100°C for 3 h | XRD |
| 6 | w/h + annealing 950°C for 25 h | XRD |
| 7 | w/h + hydrogen saturation | TGA, XRD |
| 8 | w/h + hydrogen saturation + annealing 900°C for 3 h | XRD |
| 9 | w/h + hydrogen saturation + annealing 950°C for 3 h | XRD |

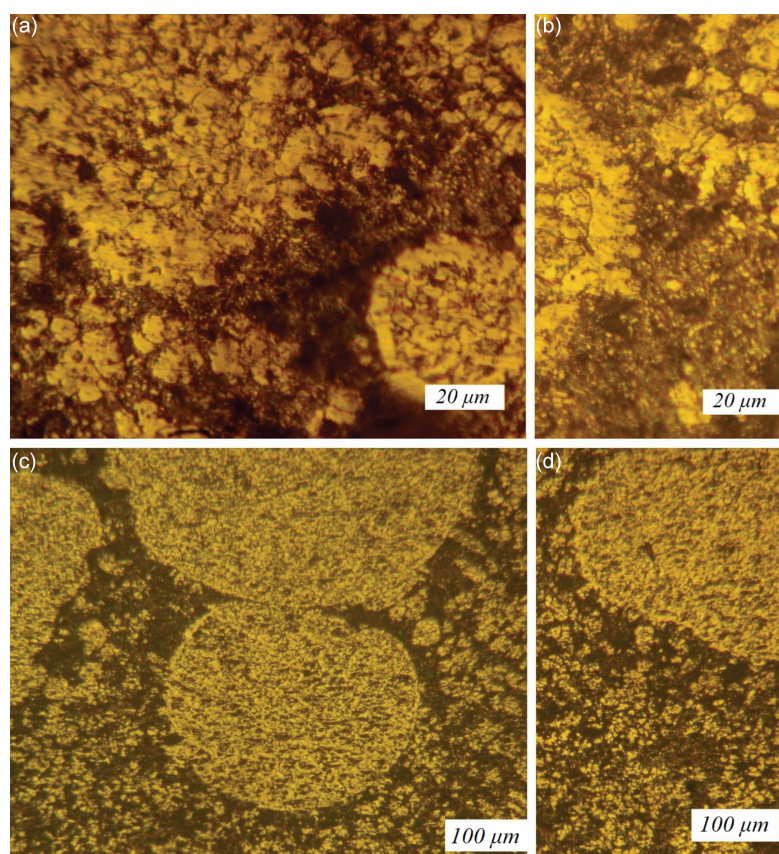


Fig. 7. Microstructure of 65Y35Ti ingot at different magnifications (black color corresponds to etched yttrium).

the tape without hydrogen saturation begins at lower temperatures. The average value of the temperature difference of intensive oxidation is about 70°C.

X-ray diffraction analysis of sample no. 1 showed (Fig. 9) that according to the state diagram, the bands also consist of two separate phases — almost pure α -Ti and almost pure yttrium. The weight content of the phases, calculated from the diffraction pattern, coincides with the initial composition (35.5 wt% Ti and 64.5 wt% Y). Parameters of the yttrium phase lattice are $a = 3.653 \text{ \AA}$, $c = 5.738 \text{ \AA}$ and of the titanium phase

— $a = 2.956 \text{ \AA}$, $c = 4.683 \text{ \AA}$, with tabular values, respectively, $a = 3.6471 \text{ \AA}$, $c = 5.7285 \text{ \AA}$ and $a = 2.905 \text{ \AA}$, $c = 4.682 \text{ \AA}$.

The discrepancy between the experimental data and the tabular data can be explained by the presence of impurities with an atomic radius smaller than the atomic radius of yttrium, so the experimental values smaller than the tabular values for yttrium and titanium impurities with a large atomic radius.

Table IV shows the phase composition and the size of the coherent scattering region (CSR) of the samples studied.

TABLE IV

Phase composition and size of CSR of the tested samples. Note: * — CSR was not measured; ** — large crystal sample.

| Sample no. | Processing | Phase | Weight content [wt%] | Size of CSR [nm] |
|------------|--|--|----------------------|------------------------|
| 1 | Quickly hardened | Y Ti- α | 64.5 35.5 | 36.5 18.7 |
| 2 | Annealing 900°C for 3 h | Y ₂ Ti ₂ O ₇ Y ₂ O ₃ TiO ₂ -ru | 55.4 23.8 20.8 | * * * |
| 3 | Annealing 950°C for 3 h | Y ₂ Ti ₂ O ₇ Y ₂ O ₃ TiO ₂ -ru | 93.6 3.5 2.9 | 95.3 * * |
| 4 | Annealing 1000°C for 3 h | Y ₂ Ti ₂ O ₇ | 95.9 | 307.9 |
| 5 | Annealing 1100°C for 3 h | Y ₂ Ti ₂ O ₇ | ≈ 100 | ** |
| 6 | Annealing 950°C for 25 h | Y ₂ Ti ₂ O ₇ | ≈ 100 | 176.3 |
| 7 | w/h + hydrogen saturation | YH ₂ TiH ₂ | 64.57 35.43 | 38.5 23.2 |
| 8 | w/h + hydrogen saturation + annealing 900°C for 3 h | Y ₂ Ti ₂ O ₇ Y ₂ O ₃ TiO ₂ -ru | 48.4 30.7 20.9 | 59.2 59.6 440.8 |
| 9 | w/h + hydrogen saturation + annealing 950°C for 3 h | Y ₂ Ti ₂ O ₇ Y ₂ O ₃ TiO ₂ -ru | 81.8 10.0 8.2 | 132.8 58.5 639.3 |

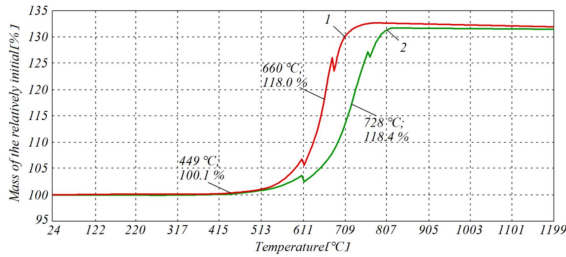


Fig. 8. Thermogravimetric comparison of fast-hardened strips with and without hydrogenation: 1 — strip w/h (sample no. 1); 2 — strip w/h + H₂ (sample no. 7).

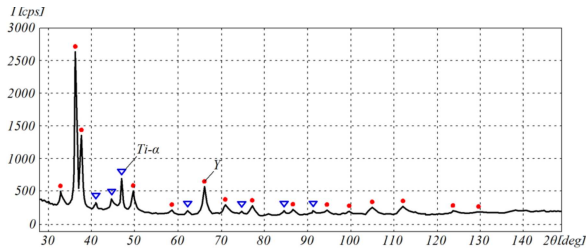


Fig. 9. Diffractogram of the sample no. 1.

The data show that the size of CSR (grain) depends more on temperature than on the annealing time. Thus, an increase in temperature from 950

to 1000°C at the same exposure time (3 h) did not lead to a significant change in the amount of pyrochlorine, but the size of CSR increased three-fold. In addition, hydrogen saturation reduces the efficiency of pyrochlorine synthesis and increases the grain size, which may be associated with grain growth at the stage of hydrogen saturation.

Comparisons of samples no. 3 and no. 6 show that the exposure time plays a minor role for this technology. Thus, with an eightfold increase in the aging time, the grain size increased by less than 2 times.

4. Conclusion

Studies have shown the following:

- heating the mixture of oxides Y₂O₃ and ZrO₂ to 2915°C with subsequent melting leads to the synthesis of a homogeneous complex ternary oxide with the fluorite structure;
- additional annealing of the melted samples at the temperature of 1200°C for 7 h in air does not lead to the formation of other phases, in particular with the structure of pyrochlorine;
- in contrast to the low-temperature methods of complex compounds synthesis, after melting according to the tested technology, the samples recorded a pure phase of fluorite without impurities of the original oxides;

- the oxidation technology of fast-hardened Y–Ti equiatomic alloy strips makes it possible to obtain pyrochlorine particles with a particle size of about 100 nm and can be used to obtain nanomodifiers of DSO-steels;
- hydrogen saturation after rapid hardening does not make technological sense and leads to deterioration of the final result;
- to obtain nanosized particles $Y_2Ti_2O_7$ from fast-hardened tapes, the following technological parameters can be recommended: annealing temperature 900–950°C and holding time from 10 to 20 h.

Acknowledgments

The article was prepared as part of a study under the state budget topic The Use of Non-traditional Methods of Obtaining Nanopowders and Sintering in the Development of Modified Mullite-ZrO₂ Ceramics Resistant to Heat Shock (State Registration Number 0121U109441) with the financial support of the Ministry of Education and Science of Ukraine.

References

- [1] E. Gevorkyan, J. Chmiel, B. Wiśnicki, T. Dzhuguryan, M. Rucki, V. Nerubatskyi, *Energies* **15**, 6443 (2022).
- [2] V.O. Chyshkala, S.V. Lytovchenko, E.S. Gevorkyan, V.P. Nerubatskyi, O.M. Morozova, *SWorldJournal* **7**, 17 (2021).
- [3] S.A. Kramer, H.L. Tuller, *Solid State Ion.* **82**, 15 (1995).
- [4] T. Norby, *J. Mater. Chem.* **11**, 11 (2001).
- [5] F.W. Shi, X.J. Meng, G.S. Wang, T. Lin, J.H. Ma, Y.W. Li, J.H. Chu, *Condens. Matter* **370**, 277 (2005).
- [6] G.R. Lumpkin, M. Pruneda, S. Rios, K.L. Smith, K. Trachenko, K.R. Whittle, N.J. Zaluzec, *J. Solid State Chem.* **180**, 1512 (2007).
- [7] R. Vassen, D. Sebold, D. Stoeber, *Ceram. Eng. Sci. Proc.* **28**, 27 (2008).
- [8] W. Ren, S. Trolier-McKinstry, C.A. Randall, T.R. Shrout, *J. Appl. Phys.* **89**, 767 (2001).
- [9] B.J. Wuensch, K.W. Eberman, C. Heremans, E.M. Ku, P. Onnerud, E.M. Yeo, S.M. Haile, J.K. Stalick, J.D. Jorgensen, *Solid State Ion.* **129**, 111 (2000).
- [10] R.C. Ewing, W.J. Weber, J.Lian, *J. Appl. Phys.* **95**, 5949 (2004).
- [11] F. Matteucci, G. Cruciani, M. Dondi, G. Baldi, A. Barzanti, *Acta Mater.* **55**, 2229 (2007).
- [12] M. Kumar, I. Arul Raj, R. Pattabiraman, *Mater. Chem. Phys.* **108**, 102 (2008).
- [13] M.P. Schmitt, A.K. Rai, R. Bhattacharya, D. Zhu, D.E. Wolfe, *Surf. Coat. Technol.* **251**, 56 (2014).
- [14] S.V. Lytovchenko, E.S. Gevorkyan, V.P. Nerubatskyi, V.O. Chyshkala, L.V. Voloshyna, *J. Superhard Mater.* **44**, 176 (2022).
- [15] D. Shin, H.-G. Shin, H. Lee, *Calphad* **45**, 27 (2013).
- [16] X. Fang, *Int. J. Hydrogen Energy* **41**, 11141 (2016).
- [17] P.K. Schelling, S.R. Phillpot, R.W. Grimes, *Philos. Mag. Lett.* **84**, 127 (2004).
- [18] B. Liu, J.Y. Wang, Y.C. Zhou, T. Liao, F.Z. Li, *Acta Mater.* **55**, 2949 (2007).
- [19] K.B. Helean, S.V. Ushakov, C.E. Brown, A. Navrotsky, J. Lian, R.C. Ewing, J.M. Farmer, L.A. Boatner, *J. Solid State Chem.* **177**, 1858 (2004).
- [20] H. Lei, Y. Sun, X. Zhu, W. Song, J. Yang, H. Gu, *IEEE Trans. Appl. Supercond.* **17**, 3819 (2007).
- [21] L.F. He, J. Shirahata, T. Nakayama, T. Suzuki, H. Suematsu, I. Ihara, Y.W. Bao, T. Komatsu, K. Niihara, *Scr. Mater.* **64**, 548 (2011).
- [22] T. Jeyasingh, S.K. Saji, V.T. Kavitha, P.R.S. Wariar, *Int. J. Adv. Res. Sci. Eng.* **06**, 87 (2017).
- [23] L. Kong, Y. Zhang, I. Karatchevtseva, *J. Nucl. Mater.* **494**, 29 (2017).
- [24] Q.A. Li, W.S. Rong, H.F. Run, G. Takashi, *Mater. Sci. Forum* **1035**, 663 (2021).
- [25] M. Suganya, K. Ganesan, P. Vijayakumar, A.S. Gill, R. Ramaseshan, S. Ganesamoorthy, *Scr. Mater.* **187**, 227 (2020).
- [26] H.Y. Xiao, F. Gao, W.J. Weber, *Phys. Rev. B* **80**, 212102 (2009).
- [27] M.B. Johnson, D.D. James, A. Bourque, H.A. Dabkowska, B.D. Gaulin, M.A. White, *J. Solid State Chem.* **182**, 725 (2009).
- [28] Y. Jiang, J.R. Smith, G.R. Odette, *Acta Mater.* **58**, 1536 (2010).
- [29] K. Yutani, H. Kishimoto, R. Kasada, A. Kimura, *J. Nucl. Mater.* **367**, 423 (2007).
- [30] V.V. Bryk, V.N. Voevodin, A.S. Kal'chenko, V.V. Mel'nichenko, I.M. Neklyudov, V.S. Ageev, A.A. Nikitina, *VANT* **84**, 23 (2013) (in Russian).
- [31] T. Liu, L. Wang, C. Wang, H. Shen, H. Zhang, *Mater. Design*, **88**, 862 (2015).

- [32] S.V. Starostenko, V.M. Voevodin, M.A. Tykhonovs'kyi, M.I. Danilenko, O.S. Kal'chenko, O.M. Velykodnyi, N.F. Andrievs'ka, *Mater. Sci.* **51**, 827 (2016).
- [33] O.M. Velikodnii, V.M. Voevodin, M.A. Tikhonovs'kii, V.V. Brik, O.S. Kal'chenko, S.V. Starostenko, I.V. Kolodii, V.S. Okovit, O.M. Bovda, L.V. Onishchenko, G.E. Storozhilov, *VANT* **92**, 94 (2014).
- [34] S.V. Starostenko, V.M. Voevodin, O.S. Kal'chenko, O. M. Velikodnii, M.A. Tikhonovs'kii, *VANT* **104**, 3 (2016).
- [35] E. Gevorkyan, V. Nerubatskyi, V. Chyshkala, Y. Gutsalenko, O. Morozova *East.-Eur. J. Enterp. Technol.* **6**, 40 (2021).
- [36] E.S. Gevorkyan, M. Rucki, A.A. Kagramanyan, V.P. Nerubatskiy, *Int. J. Refract. Met. Hard Mater.* **82**, 336 (2019).
- [37] E. Gevorkyan, V. Nerubatskyi, V. Chyshkala, O. Morozova, *East.-Eur. J. Enterp. Technol.* **5**, 6 (2021).
- [38] E. Gevorkyan, A. Mamalis, R. Vovk, Z. Semiatkowski, D. Morozow, V. Nerubatskyi, O.M. Morozova, *J. Instrum.* **16** P10015 (2021).
- [39] Z. Krzysiak, E. Gevorkyan, V. Nerubatskyi, M. Rucki, V. Chyshkala, J. Caban, T. Mazur, *Materials* **15**, 6073 (2022).
- [40] E. Gevorkyan, M. Rucki, T. Sałaciński, Z. Siemiątkowski, V. Nerubatskyi, W. Kucharczyk, Y. Chrzanowski, Y. Gutsalenko, M. Nejman, *Materials* **14**, 3432 (2021).
- [41] E. Gevorkyan, V. Nerubatskyi, Y. Gutsalenko, O. Melnik, L. Voloshyna, *East.-Eur. J. Enterp. Technol.* **6**, 41 (2020).
- [42] E. Gevorkyan, M. Rucki, Z. Krzysiak, V. Chyshkala, W. Zurowski, W. Kucharczyk, V. Barsamyan, V. Nerubatskyi, T. Mazur, D. Morozow, Z. Siemiątkowski, J. Caban, *Materials* **14**, 6503 (2021).